Journal of Polymer Science

WILEY

JOURNAL OF POLYMER SCIENCE

RESEARCH ARTICLE OPEN ACCESS

pH and Temperature Dependence of Low-Core T_g Micellar Structures Formed by PDMAEMA-*b*-PLMA Diblock Copolymers in Aqueous Solution

Varvara Chrysostomou[1] | Stefano Da Vela[2] | Stergios Pispas[1] | Christine M. Papadakis[3]

[1]Theoretical and Physical Chemistry Institute, National Hellenic Research Foundation, Athens, Greece | [2]European Molecular Biology Laboratory (EMBL), Hamburg Unit c/o Deutsches Elektronen-Synchrotron, Hamburg, Germany | [3]Technical University of Munich, TUM School of Natural Sciences, Physics Department, Soft Matter Physics Group, Garching, Germany

Correspondence: Stergios Pispas (pispas@eie.gr) | Christine M. Papadakis (papadakis@tum.de)

Received: 30 November 2024 | **Revised:** 16 January 2025 | **Accepted:** 17 January 2025

Keywords: amphiphilic block copolymers | light scattering | self-assembly | synchrotron small-angle X-ray scattering

ABSTRACT

A diblock copolymer featuring a hydrophobic block with a low glass transition temperature and a pH-responsive, cationic block is synthesized and investigated with respect to its self-assembly behavior in aqueous solution. The synthesis of the poly(lauryl methacrylate)-*block*-poly(2-(*N*,*N*-dimethylamino) ethyl methacrylate) diblock copolymer $PDMAEMA_{60}$-*b*-$PLMA_{40}$ is carried out using reversible addition fragmentation chain transfer (RAFT) polymerization. Its self-assembly in dilute aqueous solution at pH 7 is investigated using various light scattering methods. Micelles with a positive zeta potential are identified. Synchrotron small-angle X-ray scattering reveals changes in the inner structure of the micelles as a function of temperature and at pH values above, below and close to the p*K*a value of PDMAEMA (ca. 7.5). At all pH values, cigar-shaped core–shell micelles are found. While the micellar size and shape hardly change with temperature at pH 5, temperature responsivity is observed at pH 7 and 10, resulting in, among others, a change of the core size. These structural changes are facilitated by the softness of the PLMA core. Such systems may be suitable for the co-delivery of hydrophobic drugs and nucleic acids.

1 | Introduction

Self-assembled micelles from amphiphilic block copolymers with a hydrophobic core and a (permanently) hydrophilic shell have been prepared from a variety of block copolymers and have, for instance, been proposed as nanocarriers for hydrophobic drugs long time ago [1, 2]. More functional, "smart" systems have been created by using diblock copolymers having—instead of a permanently water-soluble block—a charged or even pH-responsive shell-forming block [1]. Depending on the composition and the pH value, such diblock copolymers self-assemble into a number of nanostructures, such as spheres, rods, vesicles, tubules or disks; thus, they afford a large variety of delivery systems [2–8]. However, many of these systems feature hydrophobic blocks, such as polystyrene or poly(methyl methacrylate), which have a high glass temperature, that is, significantly higher than room temperature. The restricted mobility of the core blocks at room temperature may result in difficulties to reach the equilibrium self-assembled structure, resulting in trapped states. Moreover, in medical applications that involve soft tissue, it may be advantageous to have more flexible systems available.

A system that features a soft hydrophobic core and a pH-responsive shell was designed from diblock copolymers with a hydrophobic poly(lauryl methacrylate) (PLMA) block and a pH-responsive poly(2-(*N*,*N*-dimethylamino) ethyl methacrylate) (PDMAEMA) block [9]. PLMA is biocompatible (FDA approved) and, as such, suitable for medical applications [10]. Due to its long aliphatic side chain, PLMA is strongly hydrophobic. As its glass transition temperature T_g is well below

room temperature ($T_g = -53°C$) [11], the blocks exhibit a certain mobility at room and physiological temperatures. Hence, the core is soft, which facilitates equilibration. PDMAEMA is a weak cationic polyelectrolyte with a pK_a of ca. 7.5, meaning that its water solubility, charge, and chain conformation can be controlled by pH [12]. For pH values between 7 and 10, it features lower critical solution temperature (LCST) behavior, with cloud points decreasing from ca. 80°C to ca. 40°C at the higher pH. Moreover, it is biocompatible. A previous investigation by some of us addressed the role of molar mass and composition of a series of diblock copolymers of the type PDMAEMA-*b*-PLMA [9]. In aqueous solution, these were found to form micelles that are responsive to pH, temperature, and ionic strength. The effect of varying the pH value was investigated using a PDMAEMA-*b*-PLMA diblock copolymer with a $M_w = 18{,}000\,g\,mol^{-1}$ and a weight fraction of PLMA (w_{PLMA}) = 0.23. A strong pH dependence of self-assembly behavior was observed: While the polymers are molecularly dissolved as unimers in aqueous solution at pH 3, self-assembled micelles are formed at pH 7, and clusters of micelles are formed at pH 10. The ability to dissolve into unimers at low pH values was ascribed to the disruption of the fluid micellar PLMA cores. The clustering of the micelles at pH 10 was attributed to the reduced water solubility of the PDMAEMA blocks in the uncharged state [9]. The zeta potential was found to be positive at pH 3 and 7, which was attributed to the protonation of PDMAEMA. A negative value was found at pH 10, which was attributed to the deprotonation of PDMAEMA and the presence of carboxyl end groups from the chain transfer agent (CTA). Similar findings were reported for other PDMAEMA-*b*-PLMA diblock copolymers having different compositions and overall molar masses [9]. An increase in temperature was found to result in a significant decrease in the hydrodynamic radius of the micelles, which was attributed to the shrinkage of the PDMAEMA shell due to the reduced water solubility of the PDMAEMA blocks upon heating [9].

In the present study, we present the synthesis, molecular characterization, and self-assembly behavior of a PDMAEMA$_{60}$-*b*-PLMA$_{40}$ diblock copolymer. Its molar mass is chosen to be higher than for the previously investigated ones [9], which is expected to prevent the decomposition of the micelles at low pH values. The self-assembly behavior is characterized in dilute aqueous solution at pH 7, specifically with respect to the CMC, the overall micellar size, and the zeta potential. The micellar structures are investigated in detail in dilute aqueous solution at pH values of 5, 7, and 10, and at temperatures ranging between 25°C and 50°C, using synchrotron small-angle X-ray scattering (SAXS). Structural changes in the micelles are observed due to the conformational changes of the PDMAEMA corona chains as solution conditions are altered, a process further promoted by the low T_g characteristics of the PLMA hydrophobic chains in the micellar core.

2 | Results and Discussion

2.1 | Synthesis and Molecular Characterization of the PDMAEMA-*b*-PLMA Diblock Copolymer

A PDMAEMA-*b*-PLMA diblock copolymer was synthesized via reversible addition-fragmentation chain transfer (RAFT) polymerization, following a two-step synthetic procedure as described in our previous work [9] and in the Supporting Information (SI). A PDMAEMA homopolymer was synthesized first and was used as a macro-CTA for the polymerization of the second PLMA block. The synthetic route and the chemical structure of the block copolymer are shown in Scheme 1. The synthesized homopolymer and diblock copolymer were molecularly characterized by size exclusion chromatography (SEC), and their molecular characteristics are presented in Table 1. The resulting molecular masses are close to the stoichiometric ones,

TABLE 1 | Molecular characteristics of the polymers under investigation.

Sample	M_w [a] ($g\,mol^{-1}$)	M_w/M_n [a]	NMR ratio [b] (%wt)	Yield (%)
PDMAEMA	9700	1.17	—	90
PDMAEMA$_{60}$-*b*-PLMA$_{40}$	19,600	1.27	48:52	98

[a]Determined by size exclusion chromatography.
[b]Determined by ^{1}H-NMR.

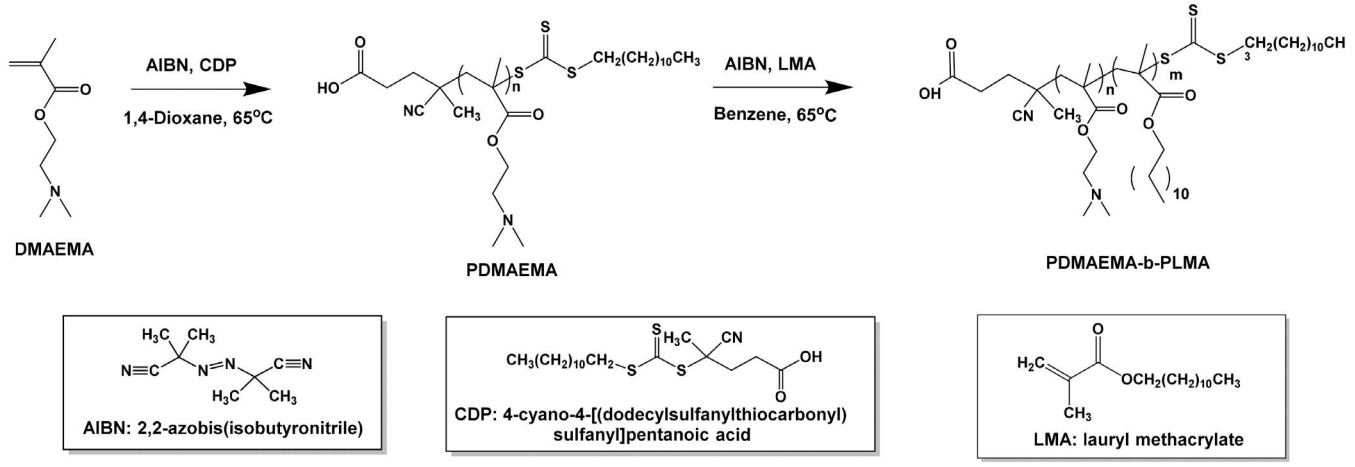

SCHEME 1 | Synthetic route for the synthesis of the PDMAEMA-*b*-PLMA diblock copolymer.

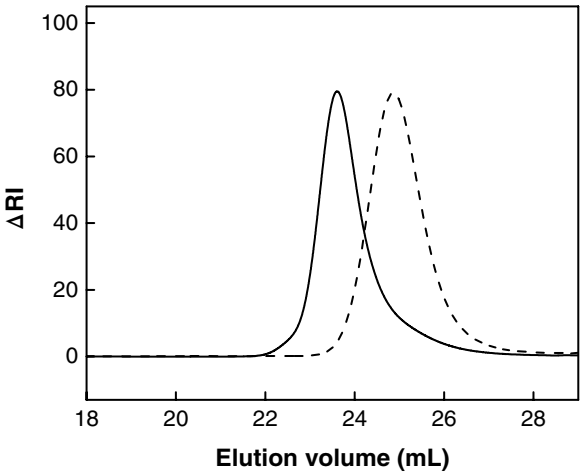

FIGURE 1 | SEC chromatograms of the PDMAEMA homopolymer (dashed line) and the PDMAEMA-*b*-PLMA diblock copolymer (solid line) in THF/5%v/v Et_3N, using a differential refractive index (RI) detector.

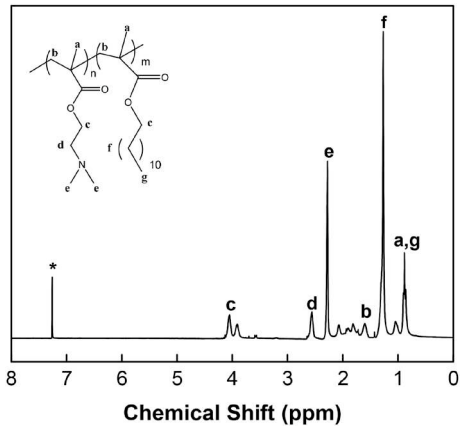

FIGURE 2 | ^{1}H-NMR spectrum of the PDMAEMA-*b*-PLMA diblock copolymer in $CDCl_3$. The peak at 7.26 ppm, denoted by (*), is assigned to the solvent protons.

and the dispersity index values (M_w/M_n) are within a satisfactory range for RAFT polymerization procedures. Figure 1 presents the chromatograms of the PDMAEMA-*b*-PLMA copolymer and the PDMAEMA precursor. The chromatograms of both polymers show narrow, monomodal, and symmetric distributions. Moreover, the chromatogram of the PDMAEMA-*b*-PLMA copolymer is shifted to a smaller elution volume compared to the precursor, indicating an increase in molar mass. Consequently, the chromatograms and the obtained data correspond to well-defined polymers, demonstrating a controlled synthetic procedure through the RAFT polymerization scheme utilized.

The confirmation of the chemical structure and the determination of the composition of the PDMAEMA-*b*-PLMA diblock copolymer were performed by proton nuclear magnetic resonance (^{1}H-NMR) spectroscopy. Spectrum analysis (see the SI) verified the expected chemical structure (Figure 2). The composition was evaluated using the characteristic spectral peaks at 2.32 ppm, corresponding to the ━CH_3 protons of the amino group (peak e, 6H, ━$N(CH_3)_2$) of PDMAEMA, and at 1.26 ppm,

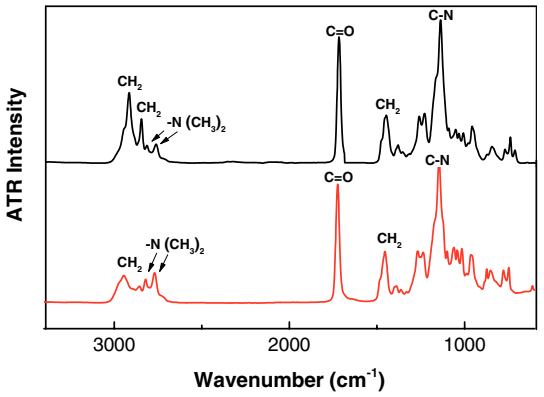

FIGURE 3 | ATR-FTIR spectra of the PDMAEMA homopolymer (lower red line) and the PDMAEMA-*b*-PLMA diblock copolymer (upper black line) in the solid state.

which corresponds to the ━CH_2 protons of the PLMA side chain (peak f, 2H, ━$CH_2(CH_2)_{10}CH_3$━) [9]. According to the obtained results, the composition was found to be close to the theoretical one and is presented in Table 1.

Additionally, Fourier-transform infrared spectroscopy (FTIR) was used to confirm the chemical structure of the synthesized polymers. Representative FTIR spectra of the PDMAEMA-*b*-PLMA diblock copolymer and the PDMAEMA precursor are presented in Figure 3. The spectral features of both polymers are similar to those described in detail in our previous work [9], including all the characteristic bands that demonstrate the expected chemical structure of the synthesized PDMAEMA-*b*-PLMA diblock copolymer and also of the PDMAEMA homopolymer.

2.2 | Self-Assembly of the PDMAEMA-*b*-PLMA Diblock Copolymer in Aqueous Solution

Studies on the ability of the PDMAMEA-*b*-PLMA diblock copolymer to self-assemble into micelles in aqueous solution were performed by determining the critical micelle concentration (CMC) using fluorescence spectroscopy. Pyrene was used as the fluorescent probe due to its hydrophobic character, its sensitivity to micropolarity variations, and its ability to be encapsulated in the hydrophobic micellar core. The intensities of the characteristic vibronic peaks, I_1 and I_3, in the pyrene emission spectrum were used to determine the CMC. A representative fluorescence spectrum of pyrene in an aqueous polymer solution with a concentration of 1 g L^{-1}, as well as the utilized characteristic peaks, is shown in Figure 4a. The fluorescence intensity ratio of the pyrene peaks, I_1/I_3, is plotted against the copolymer concentration of the prepared aqueous solutions, ranging from 10^{-8} to 10^{-3} g mL^{-1} in Figure 4b. The plateau observed at low concentrations indicates that the micelles have not formed yet, while the transition region at intermediate concentrations and the plateau at higher concentrations reveal their efficient formation. The CMC value is determined as the inflection point of the curve, as shown in Figure 4b, and is listed in Table 2.

The self-assembly behavior of the amphiphilic PDMAEMA-*b*-PLMA diblock copolymer in aqueous solution was investigated using light scattering techniques. Dynamic light scattering

(DLS) was performed to determine the hydrodynamic radii, R_h, and the polydispersity index (PDI) of the micelles. Figure 5 shows the intensity-weighted distribution of hydrodynamic radii from the CONTIN analysis of the intensity autocorrelation functions measured at a scattering angle 90° for an aqueous solution of the PDMAEMA-*b*-PLMA diblock copolymer at a polymer concentration of 1 g L^{-1}. The monomodal, narrow, and symmetrical size distribution indicates that well-defined micellar structures are formed. Using the cumulant method on the data at 90°, the average hydrodynamic radius, R_h, of the micelles was found to be 43 nm, with a PDI of 0.18 (Table 2). These structures are expected to be composed of a hydrophobic PLMA core and a hydrophilic PDMAEMA shell.

Static light scattering (SLS) was employed to determine the radius of gyration of the micelles, R_g, which was found to be 61 nm. The Zimm second-order analysis method was used in the angular range of 30°–150° (Figure 6). The R_g/R_h ratio was determined using the extrapolated value of R_{h0} and was found to be 1.06. This value indicates the formation of somewhat elongated micelles, which is consistent with the relatively high content of the hydrophobic PLMA block and the long aliphatic side chains of PLMA, which may not be able to pack well in a spherical core. Moreover, the hydrodynamic radius from DLS, which is larger than the calculated contour length of the copolymer, $L = 25$ nm, supports the formation of micelles with an elongated morphology. The values obtained from SLS are included in Table 2.

The surface charge of the micellar structures was determined by electrophoretic light scattering (ELS). The zeta potential ζ_p assumes a positive value ($\zeta_p = +35$ mV), as expected from the partially charged tertiary amine groups of PDMAEMA at pH 7.

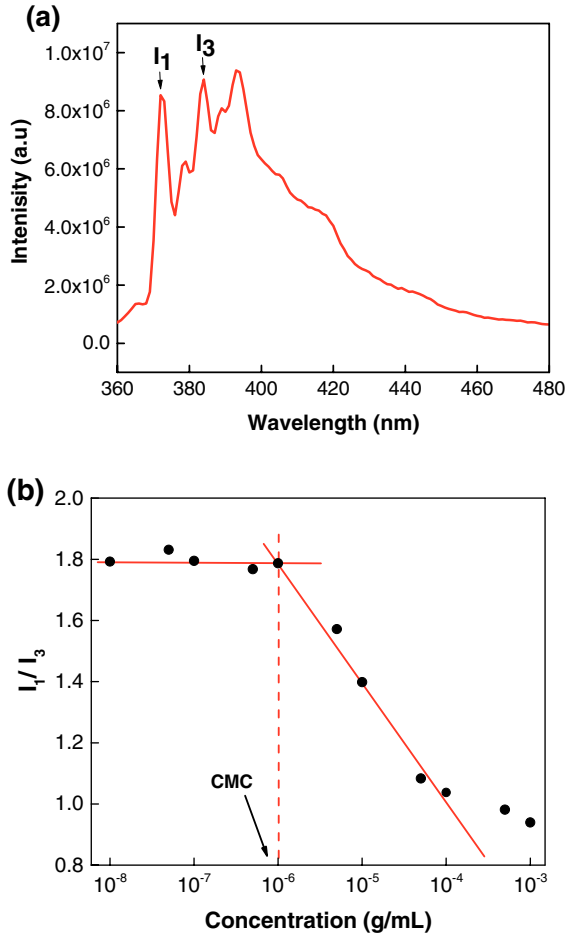

FIGURE 4 | (a) Representative fluorescence spectrum of an aqueous PDMAEMA-*b*-PLMA/pyrene solution at a polymer concentration of 1 g L^{-1}. (b) Determination of the critical micelle concentration (CMC) of PDMAEMA-*b*-PLMA in aqueous solutions, using pyrene as a fluorescent probe at 25°C and pH 7. The crossover point of the fitted lines (red solid lines) indicates the CMC value, which is indicated by the vertical red dashed line.

2.3 | Shape and Inner Structure of the Micelles Formed by the PDMAEMA-*b*-PLMA Diblock Copolymer in Aqueous Solution

The micellar structures, that is, the size, shape, inner structure, and aggregation, were determined using synchrotron SAXS.

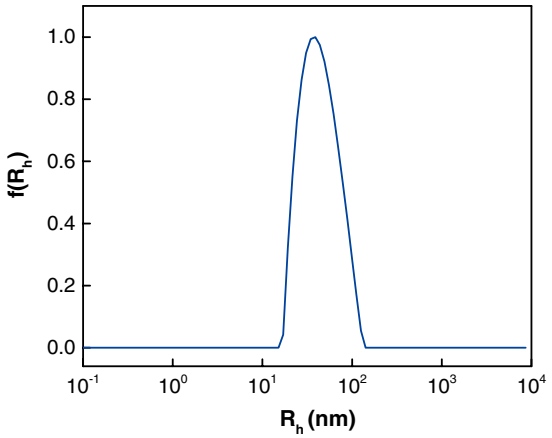

FIGURE 5 | Size distribution from a CONTIN analysis of the DLS intensity autocorrelation function of an aqueous solution of the PDMAEMA-*b*-PLMA diblock copolymer at a concentration of 1 g L^{-1} at pH 7, measured at 90°.

TABLE 2 | Structural characteristics of the micelles formed by PDMAEMA-*b*-PLMA in aqueous solution (H_2O) at a concentration of 1 g L^{-1} and pH 7.

Sample	R_h [a] (nm)	PDI[a]	R_g [b] (nm)	R_g/R_{h0} [c]	CMC[d] (10^{-3} g L^{-1})	ζ_p [e] (mV)
$PDMAEMA_{60}$-*b*-$PLMA_{40}$	43	0.18	61	1.06	1.06	+35

[a]Determined by cumulant analysis on DLS data measured at 90°.
[b]Determined by SLS.
[c]Determined by multi-angle DLS after extrapolation to zero angle, $R_{h0} = 57.5$ nm.
[d]Obtained from fluorescence spectroscopy.
[e]Determined by ELS.

Solutions with a concentration of 10 g L^{-1} were prepared in D_2O at pH 5, 7, and 10. This concentration was chosen to be low to minimize intermicellar interactions, while still providing sufficient scattering signal. D_2O was used for consistency with planned neutron scattering experiments. Typically, no significant deviations from the behavior in H_2O are observed. At each pH value, temperature scans were carried out from 25°C to 50°C. The resulting curves are shown in Figure 7a–c. At all pH values, the curves show a decay up to ca. 0.1 nm^{-1}, a maximum at 0.2–0.35 nm^{-1}, a shoulder, and then a decay.

At 25°C, the peak and the shoulder are the least pronounced at a pH value of 5. At pH 7, the peak is nearly at the same position as at pH 5, but the shoulder is more pronounced, and a low-q slope indicative of large aggregates appears. At pH 10, the peak is shifted to a significantly higher q value (from 0.23 nm^{-1} at pH 5 and 7 to 0.34 nm^{-1} at pH 10), the shoulder is most pronounced, and a low-q upturn is again visible. At $q > 3\ nm^{-1}$, shallow maxima are observed, which are most pronounced at pH 7 and 10. These are perhaps due to local structural features, such as ion association or correlations between chemical moieties of the polymers, and are not taken into account in the analysis.

At pH 5, essentially no change with temperature is observed (Figure 7a). In contrast, at pH 7, the intensity decreases in the q-range up to ca. 0.1 nm^{-1}, while the remainder of the data are broadly independent of temperature (Figure 7b). At pH 10, a similar decrease in intensity is observed at $q < 0.1\ nm^{-1}$, and, in addition, a noticeable shift of the peak and the shoulder to lower q values occurs as the temperature is increased. These differences point to the effect of the varying degree of ionization of the PDMAEMA blocks.

The data could be fitted with the structural model described in Section 4 (Equation 1). It includes the form factor of core–shell ellipsoids that describe the size, shape, and inner structure of the micelles. The shell thickness was assumed to be the same in all directions. In addition to the form factor, the concentration fluctuations in the micellar shell were described by an Ornstein–Zernike structure factor. We refrained from including a micelle–micelle structure factor to keep the number of fitting parameters as low as possible. The fit quality in its absence is already good, and its effects are likely to be obscured in the presence of the large aggregates present at pH 7 and 10. At pH 7 and 10, it was necessary to model additional forward scattering from aggregates formed by the micelles using a modified Porod term. We note that these aggregates are not observed in DLS experiments (Figure 5), which may be due to the lower concentration used in the DLS experiments. The fits, which were carried out using data up to $q = 3\ nm^{-1}$ (pH 5) or 2 nm^{-1} (pH 7 and 10), are throughout good

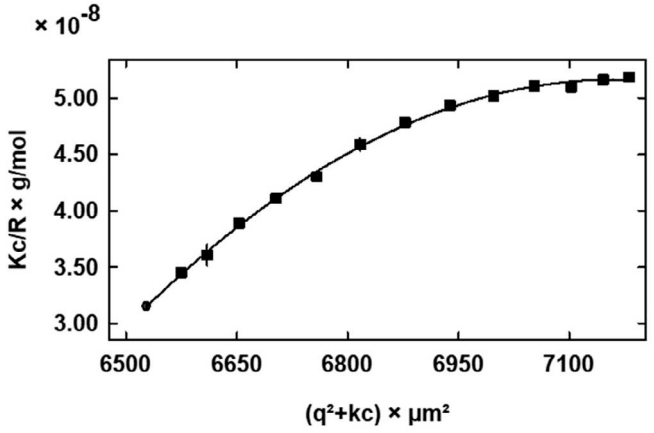

FIGURE 6 | Zimm plot from SLS on an aqueous solution of the PDMAEMA-*b*-PLMA diblock copolymer for scattering angles in the range 30°–150°. Symbols: Experimental data; line: fit.

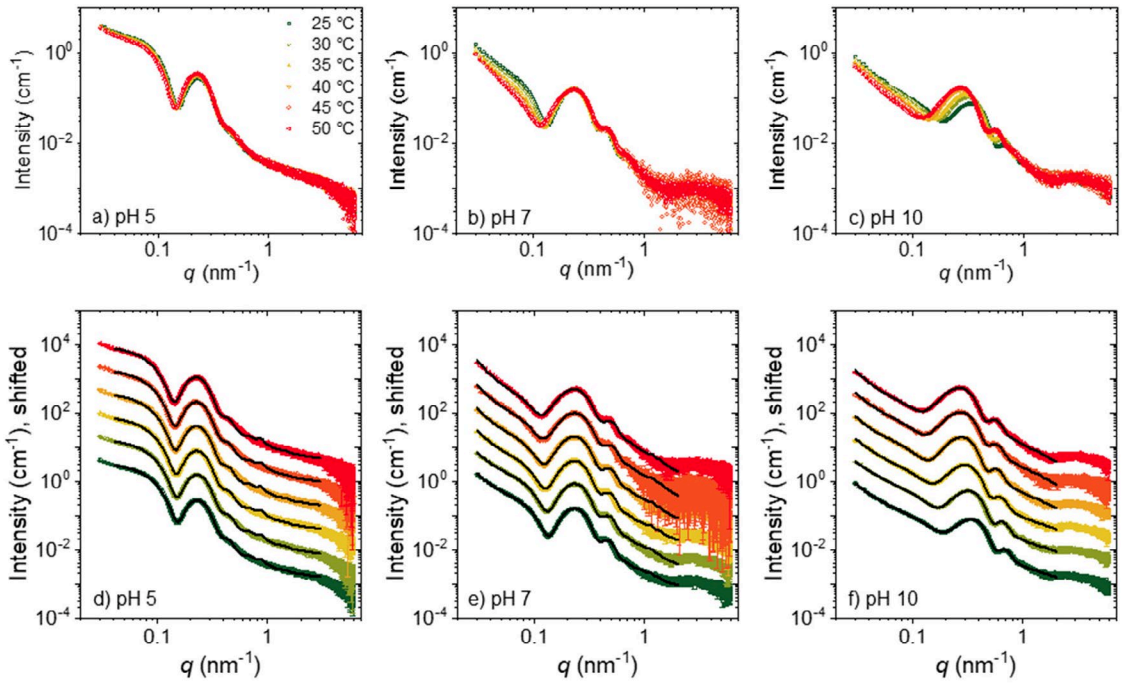

FIGURE 7 | SAXS data from the 10 g L^{-1} solution of PDMAEMA-*b*-PLMA in D_2O at pH 5 (a, d), pH 7 (b, e), and pH 10 (c, f) at the temperatures given in (a). In (d)–(f), the curves are shifted by factors of 5. Symbols: Experimental data; lines: fits of structural models, see text.

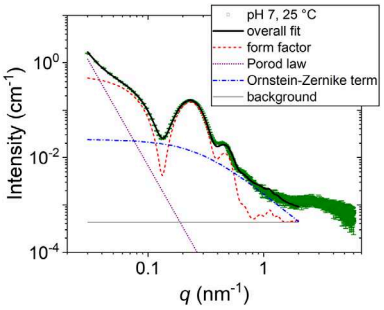

FIGURE 8 | SAXS data from the 10 g L^{-1} solution of the PDMAEMA-*b*-PLMA diblock copolymer in D_2O at pH 7° and 25°C (symbols). Only every second data point is shown. Full black line: Overall fit, see text. Dashed red line: Form factor of core–shell ellipsoids; dotted violet line: Power law; dash-dotted blue line: Ornstein–Zernike term; full gray line: Constant background.

(Figure 7d–f). The deconvolution is shown using the data at pH 7° and 25°C (Figure 8), and it reveals that the initial steep decay up to $q = 0.05\,nm^{-1}$ is mainly due to forward scattering from the large aggregates, the remaining decay, the peak, and the shoulder are attributed to the micellar form factor, and the decay at $q = 0.6–2\,nm^{-1}$ is mainly due to the concentration fluctuations.

The resulting structural parameters are compiled in Figures 9 and 10. At pH 5, the micelles have an equatorial and a polar core radius of ca. 10 and 17.5 nm, respectively (Figure 9a). Hence, the axis ratio (polar/equatorial) of the core amounts to ca. 1.7 (Figure 10a). The micellar cores, and hence the entire micelles, are thus cigar-shaped, which may be due to the rather symmetric composition (PDMAEMA:PLMA 48:52 w/w; Table 1) and possible packing constraints due to the long aliphatic side chains in PLMA. The core volume increases slightly with temperature. Assuming that the cores consist of $PLMA_{40}$ and have the same mass density as bulk PLMA, this means that the aggregation number increases from ca. 400 at 25°C to ca. 420 at 50°C. The shell thickness amounts to ca. 11 nm, giving an equatorial and a polar micellar radius of ca. 21 and 28 nm, respectively. The correlation length of concentration fluctuations, ξ, is ca. 6 nm (Figure 9a). At this temperature, the contribution of aggregates to the forward scattering is negligible, and thus, the Porod term was not needed. We conclude that, at pH 5, where the PDMAEMA block is strongly charged, rather elongated ellipsoidal core–shell micelles are formed, which consist of a few hundred diblock copolymers and do not form aggregates (Figure 11a).

At pH 7, the micelles have an equatorial core radius that decreases from 10.9 to 10.6 nm upon heating from 25°C to 50°C and a polar core radius that increases from 17.2 to 17.6 nm, respectively (Figure 9b). The axis ratio of the core increases from 1.58 at 25°C to 1.65 at 50°C (Figure 10a), that is, the core becomes slightly more elongated upon heating. The core volume decreases from $8.7 \times 10^3\,nm^3$ at 35°C to $8.3 \times 10^3\,nm^3$ at 50°C (Figure 10b), that is, the aggregation number decreases from ca. 480 to ca. 460. The shell thickness decreases from 7.9 nm at 26°C to 7.2 nm at 50°C. The equatorial micellar radius decreases from 18.9 to 17.8 nm, while the polar radius is essentially constant at 25 nm. Hence, the elliptical cores are slightly thicker than at pH 5, are less elongated, and contain more PLMA blocks. The shell is thinner than at pH 5, which is likely due to the lower degree of ionization of the

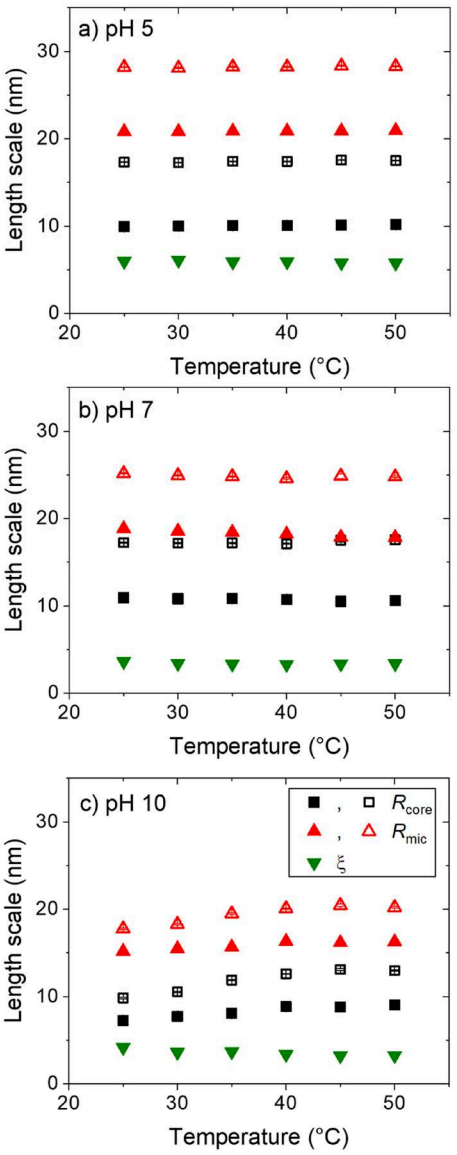

FIGURE 9 | Length scales resulting from the micellar form factor and the Ornstein–Zernike term at pH 5 (a), pH 7 (b), and pH 10 (c), as given in the legend in (c). Closed symbols: Equatorial values; open symbols: PSAXS measurements were performed on aqueous solutions with 10 g L^{-1} polymer concentration, in dependence of temperature at pH values of 5, 7, and 10. Polar values, for core (R_{core}, squares) and overall micellar radii (R_{mic}, triangles).

PDMAEMA block. The correlation length of concentration fluctuations, ξ, is ca. 3.3 nm (Figure 9b), that is, smaller than at pH 5. At pH 7, enhanced forward scattering is observed, and the Porod exponent increases from 4.3 to 4.7 upon heating (Figure 10c), while at the same time the Porod amplitude decreases slightly (Figure 10d). We conclude that, at pH 7, where the PDMAEMA block is only weakly charged, less elongated ellipsoidal core–shell micelles are formed, which have a slightly larger core volume, that is, a higher aggregation number than at pH 5. Moreover, they feature a thinner shell with a denser packing of the PDMAEMA blocks than at pH 5 (Figure 11b). Furthermore, the micelles form aggregates, which may be due to the slightly lower water solubility of the PDMAEMA shell blocks when they are less charged. The lower micellar size than observed in DLS (Table 2) may be due to the higher polymer concentration.

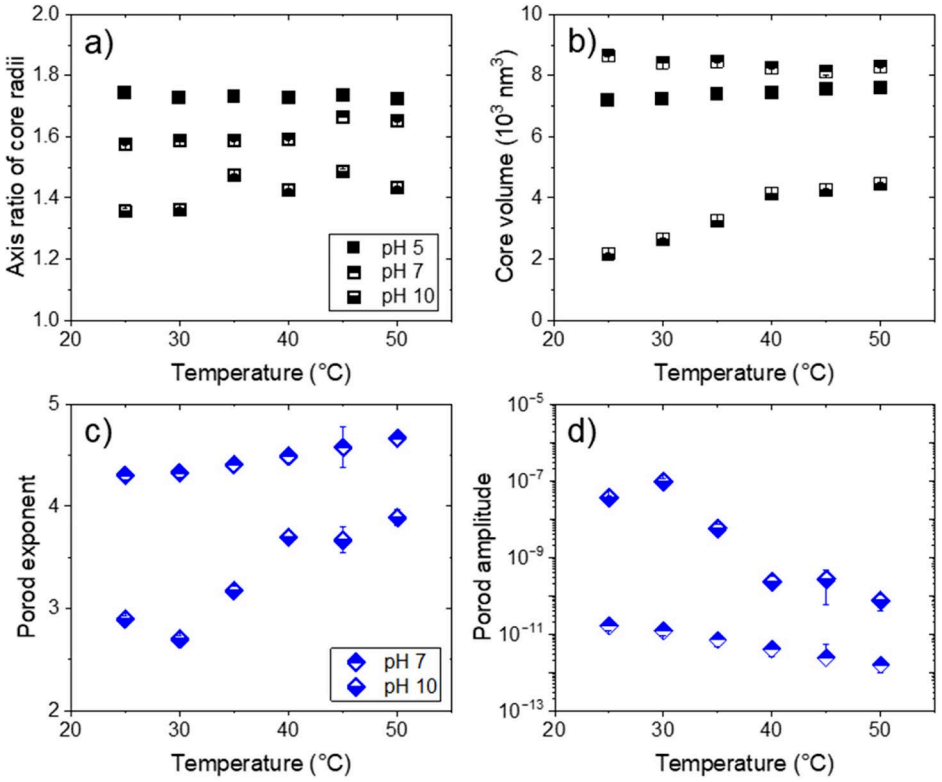

FIGURE 10 | Results from the micellar form factor: Axis ratio of the core radii (a) and the core volume (b), and from the Porod term: Porod exponent (c) and Porod amplitude (d) for pH 5 (closed symbols), pH 7 (upper half filled), and pH 10 (lower half filled).

At pH 10, the micelles have an equatorial core radius that increases from 7.3 nm at 25°C to 9.1 nm at 50°C, while the polar radius increases from 9.9 nm at 25°C to 13 nm at 50°C, respectively (Figure 9c). Hence, the axis ratio increases from 1.36 to 1.49 (Figure 10a), that is, the cores become slightly more elongated with higher temperatures. The core volume increases from 2.2×10^3 nm^3 at 25°C to 4.5×10^3 nm^3 at 50°C (Figure 10b), that is, the aggregation number increases from ca. 120 to ca. 250. The shell thickness increases from 5.6 nm at 25°C to 6.5 nm at 50°C, giving an equatorial micellar radius that increases from 15.2 nm at 25°C to 16.3 nm at 50°C and a polar micellar radius that increases from 17.8 nm at 25°C to 20.2 nm at 50°C. The correlation length of concentration fluctuations, ξ, decreases from 4.2 nm at 25°C to 3.3 nm at 50°C. The Porod exponent increases from 2.9 at 25°C to 3.9 at 50°C (Figure 10c), and the Porod amplitude is significantly higher than at pH 7 (Figure 10d). Thus, the micellar cores are significantly smaller than at pH 7, the aggregation numbers are much smaller, and the cores are less elongated. The shell is thinner than at pH 7, while the packing of the PDMAEMA blocks is equally dense, which may be attributed to the smaller core size, that is, the smaller aggregation number (Figure 11c). The large aggregates are more prominent than at pH 7. We attribute these findings to the lower degree of ionization of the PDMAEMA blocks compared topH 7 and their thermoresponsivity in the uncharged state. The fact that the core sizes are also affected points to a crosstalk between the conformation of the shell blocks and their space demand at the core–shell interface. As the shell blocks are less extended than in the charged state, their area demand is higher, which reduces the aggregation number. We hypothesize that structural transformations, such as the change in core size and the axis ratio, are facilitated also by the low T_g of the PLMA cores, which enable conformational changes of the PLMA blocks and, as a consequence, of the PDMAEMA shell blocks. Most probably, such changes would not be possible in the case of a high T_g core-forming block.

3 | Conclusions

In the present study, a diblock copolymer PDMAEMA$_{60}$-*b*-PLMA$_{40}$ with a narrow molar mass distribution was synthesized using RAFT polymerization. It is composed of a pH-responsive PDMAEMA block, which is also thermoresponsive in the uncharged state at high pH values, and a hydrophobic PLMA block, which has a glass temperature below room temperature. The successful synthesis is verified using SEC, ^{1}H-NMR, and ATR-FTIR spectroscopy. Using fluorescence spectroscopy of pyrene in aqueous solution at pH 7, the CMC is found to be ca. 10^{-3} g L^{-1}. The hydrodynamic radius of the micelles formed by the diblock copolymer in a 1 g L^{-1} solution in H_2O at pH 7 is determined by DLS to be 43 nm. Static light scattering under the same conditions reveals a radius of gyration of 61 nm and an elongated micellar shape, according to the R_g/R_h ratio. At pH 7, the zeta potential is positive, that is, the PDMAEMA block is positively charged.

SAXS measurements were performed on aqueous solutions with 10 g L^{-1} polymer concentration, in dependence on temperature at pH values of 5, 7, and 10. At pH 5, where the PDMAEMA block is strongly charged, the structures are nearly temperature-independent. Elongated ellipsoidal core–shell micelles are formed with a rather thick shell, with the core and

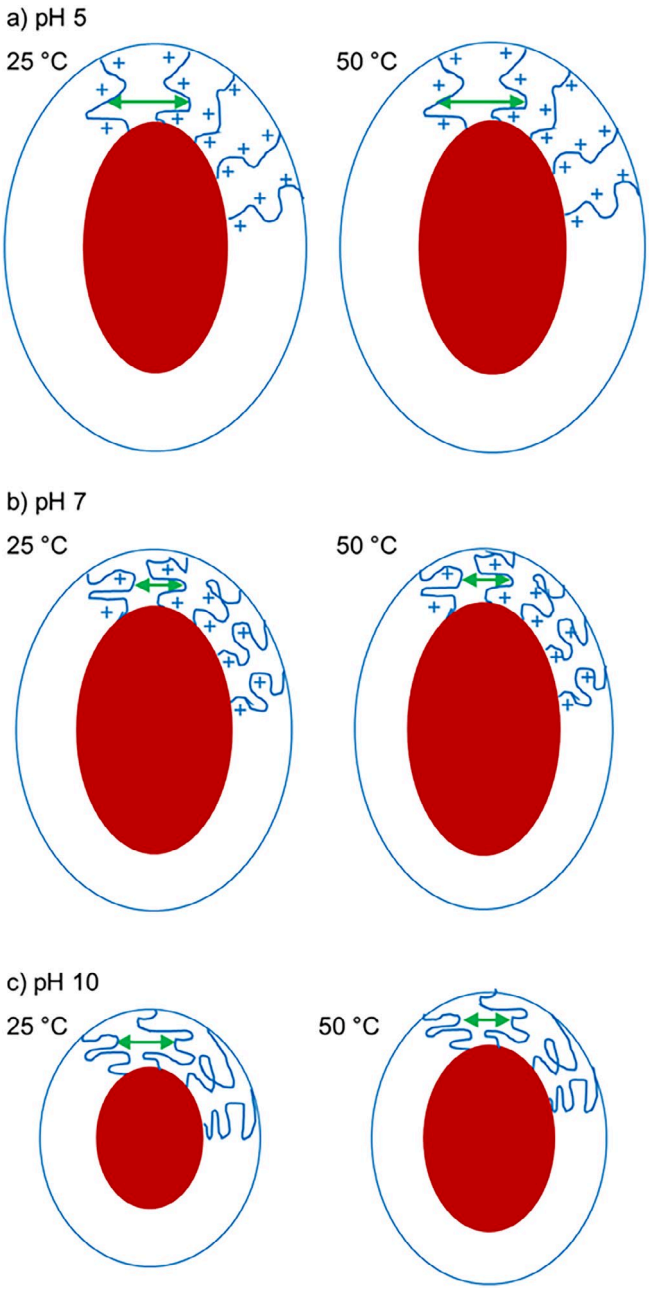

FIGURE 11 | Schematic representation of the micellar structures from SAXS at pH 5 (a), pH 7 (b), and pH 10 (c) at 25°C (left) and 50°C (right), approximately to scale. The red parts depict the micellar cores from PLMA, and the blue lines represent a few PDMAEMA blocks. These are strongly (a), weakly (b), and non-charged (c). The counterions and the water molecules are not shown. The green arrows depict the correlation length of concentration fluctuations. The large-scale aggregates formed at pH 7 and 10 are not shown.

the shell presumably formed by bulk PLMA and water-swollen PDMAEMA. At pH 7, the aspect ratio of the ellipsoids changes with temperature, and the shell thickness decreases upon heating. Moreover, aggregates formed by the micelles are observed. These temperature-dependent structural changes are attributed to the lower degree of ionization of the PDMAEMA block and its resulting thermoresponsivity, that is, the solvent quality of water becomes worse as temperature is increases. At pH 10, the micelles are significantly smaller, and the cores are less elongated. A strong increase of the core size is observed upon heating, as well as significant aggregate formation. The latter finding again reflects the thermoresponsivity of the PDMAEMA block in the uncharged state. The changes in the core size with pH value and temperature reveal that the interfacial area demand of the shell block influences the aggregation number.

The design of these block copolymers—soft hydrophobic core and positively charged shell with tunable charge—offers the possibility to create micelles that can carry both hydrophobic substances in their core and, when the shell is positively charged, at the same time complex (negatively charged) nucleic acids. Hence, they may be used to co-deliver nucleic acids for gene therapy and, for example, (hydrophobic) chemotherapeutics or contrast agents for simultaneous diagnostics [13–22]. Different from other systems, the soft core allows better adaptability to the biological environment, which may be an advantage for passing the cell membrane. Moreover, PDMAEMA is biocompatible. The pH-responsive block has the advantage that the positive charge, which is present at physiological neutral pH, may complex a nucleic acid, while it facilitates the release through the proton sponge effect [23, 24], thus avoiding degradation of the nucleic acid in lysosomes and drug elimination through the endocytic recycling pathway [15]. Additional functionalities, such as active targeting moieties, can be included [25, 26].

4 | Experimental Section

4.1 | Materials

The $PDMAEMA_{60}$-b-$PLMA_{40}$ diblock copolymer was synthesized by RAFT polymerization. Details are given in the SI. Heavy water (D_2O, purity 99.95%, from Deutero GmbH, Kastellaun, Germany), deuterated chloroform ($CDCl_3$, from Sigma-Aldrich), and tetrahydrofuran (THF, purity > 99.9%, Sigma-Aldrich) were used as received.

4.2 | Methods

4.2.1 | Molecular Characterization

The methods used for molecular characterization of the synthesized polymers are described in detail in the SI. These comprise SEC for the determination of the molar masses and the molar mass distribution, ^{1}H-NMR spectroscopy for the confirmation of the chemical structure and the determination of the composition of the copolymer, and FTIR in the form of ATR-FTIR for the verification of the chemical structure of the polymers.

4.2.2 | Fluorescence Spectroscopy

Fluorescence spectroscopy was performed to determine the CMC of the PDMAEMA-*b*-PLMA diblock copolymer in aqueous media using pyrene as the fluorescent probe. The measurements were conducted on a Fluorolog-3 Jobin Yvon-Spex spectrofluorometer (Model GL3-21). The excitation wavelength used was 335 nm, and the emission spectra were recorded in the wavelength range of 355–630 nm. For the PDMAEMA-*b*-PLMA diblock copolymer, a

stock solution in H_2O with concentration of $1\,g\,L^{-1}$ was prepared according to the co-solvent protocol as previously described [9] and as described in detail in the SI. This stock solution was diluted to give aqueous solutions with concentrations ranging from 10^{-5} to $1\,g\,L^{-1}$. Moreover, a stock solution of pyrene (1 mM) in acetone was prepared, from which 1 μL was added per 1 mL of aqueous copolymer solution. The solutions containing pyrene were left for evaporation of acetone overnight at room temperature before the fluorescence spectroscopy measurements.

4.2.3 | Light Scattering

Light scattering measurements were performed to study the self-assembly behavior of the PDMAEMA-*b*-PLMA diblock copolymer in aqueous solution to determining the size, shape, and the surface charge of the formed micellar structures. All light scattering experiments were performed at 25°C using aqueous solutions of PDMAEMA-*b*-PLMA at a concentration of $1\,g\,L^{-1}$ and pH 7 (for sample preparation see the SI).

DLS measurements were conducted on an ALV/CGS-3 compact goniometer system (ALV GmbH, Germany), equipped with a JDS Uniphase 22 mW He-Ne laser as a light source, operating at 632.8 nm, and interfaced with an ALV-5000/EPP multi-τ digital correlator with 288 channels and an ALV/LSE-5003 light scattering electronics unit for stepper motor drive and limit switch control. Moreover, a Polyscience 9102A12E bath circulator (Polyscience, Illinois, USA) was utilized to regulate the temperature inside the measuring cell. Toluene was used as the calibration standard. Before measurements, dust particles were removed by filtration of the solutions through 0.45 μm hydrophilic PVDF syringe filters (obtained from Membrane Solutions). Afterward, the solutions were put into standard 1 cm width cylindrical quartz cuvettes and equilibrated for 15 min at 25°C. The measurements were carried out at scattering angles of 30°–150° at 10° intervals. At each angle, five measurements having a duration of 30 s each were conducted. The obtained intensity correlation functions were fitted and analyzed by the CONTIN algorithm to give the distribution of decay times. Since the distribution was found to be monomodal, the hydrodynamic radii, R_h, were calculated from the peak decay time at the scattering angle of 90° via the diffusion coefficient, using the Stokes–Einstein relation. Moreover, the cumulant method was used to extract the average value of R_h and its PDI from the data measured at 90°. The R_h values obtained by the cumulant method at all measured angles were extrapolated to the value R_{h0} at 0°.

SLS measurements were performed on the same instrument in the same angular range of 30°–150° at 10° intervals, using toluene as the calibration standard. SLS intensities were analyzed by a second-order Zimm plot in order to estimate the radius of gyration, R_g, and the ratio R_g/R_{h0}.

ELS measurements were conducted using a Nano Zeta Sizer (Malvern Instruments Ltd., UK), composed of a 4 mW solid-state He-Ne laser, operated at 633 nm and at a fixed backscattering angle of 173°. The zeta potential value was determined after equilibration at 25°C using the Henry correction of the Smoluchowski equation. The recorded zeta potential values are averages of 50 scans, with an error smaller than ±2 mV.

SAXS measurements were carried out at the high-brilliance synchrotron BioSAXS EMBL beamline P12 at the Deutsches Elektronen Synchrotron (DESY), Hamburg, Germany [27]. X-rays with a wavelength $\lambda = 0.124$ nm were used, together with a sample-detector distance (SDD) of 3.0 m, resulting in a q-range of ca. $0.027–7.4\,nm^{-1}$. q denotes the momentum transfer: $q = 4\pi\sin(\theta/2)/\lambda$, where θ is the scattering angle. A 2D Pilatus 6M detector was used to record the scattered intensity, employing the scattering of silver behenate for angular calibration. Samples were centrifuged before measurements to eliminate any pre-existing large impurity or aggregates. The sample temperature was varied between 25°C and 50°C. Using a robotic sample changer (Arinax, France), the dispersions were made to flow continuously through a thermo-controlled capillary (inner diameter 1.7 mm) during illumination to reduce radiation damage [28, 29]. The samples were preliminary equilibrated in the robot sample changer and then briefly preliminary again in the capillary at the chosen temperature. Each sample was exposed 40 times for 80–100 ms each. The 2D detector maps were azimuthally averaged and were brought to absolute scale using water as a standard. After the removal of outliers, the data were averaged, and background subtraction from the respective buffer was performed, taking the transmission into account. No time dependence was observed. All operations were carried out using the software suite ATSAS 2.8 [30]. Solutions for SAXS were prepared following the method described in the SI, using THF and D_2O (D_2O was used for consistency with planned neutron scattering experiments). A $24\,g\,L^{-1}$ solution in D_2O was obtained by evaporating the THF from D_2O–THF mixtures using a rotary evaporator and further diluting to $10\,g\,L^{-1}$ with D_2O. The pH value was adjusted to 5, 7, or 10 by adding small amounts of 1 M HCl or 1 M NaOH.

4.2.4 | Analysis of the SAXS Data by Fitting Structural Model

The SAXS curves $I(q)$ were analyzed by fitting the following model:

$$I(q) = I_{agg}(q) + P(q) + I_{fluct}(q) + I_{bkg} \quad (1)$$

where $I_{agg}(q)$ denotes the scattering due to large aggregates formed by the micelles, $P(q)$ is the form factor of the micelles, $I_{fluct}(q)$ is the scattering due to concentration fluctuations in the micellar shell, and I_{bkg} is a constant background.

For $P(q)$, the form factor of randomly oriented ellipsoidal core–shell particles was used [31]. The detailed expressions are given in the SI. $P(q)$ features the equatorial radius, R_e, and the axial ratio of the core, the latter being the ratio of the polar radius of the core, R_p, to R_e. Moreover, it contains the shell thickness, t_{shell}, which was assumed to be the same in all directions, as well as the X-ray scattering length densities (SLDs) of the core, the shell, and the solvent. The SLDs of PLMA, PDMAEMA, and D_2O are 8.76×10^{-6}, 12.2×10^{-6}, and $9.33\times10^{-6}\,Å^{-1}$, as calculated from their mass densities: $\rho_{PLMA} = 0.929\,g\,cm^{-3}$, $\rho_{PDMAEMA} = 1.318\,g\,cm^{-3}$, and $\rho_{D2O} = 1.107\,g\,cm^{-3}$. The SLDs of the core and the shell were left as free fitting parameters, whereas that of the solvent was fixed at the value of D_2O.

For $I_{agg}(q)$, a modified Porod term was used:

$$I_{agg}(q) = \frac{I_p}{q^m} \quad (2)$$

with I_p a scaling factor and m the Porod exponent. The latter is indicative of the surface properties of the aggregates: [32] $m = 4$ stands for a smooth surface, $3 < m < 4$ represents rough surfaces, and $m > 4$ is obtained for surfaces with a concentration gradient [33, 34].

For $I_{fluct}(q)$, the Ornstein–Zernike structure factor was used: [35]

$$I_{fluct}(q) = \frac{I_{OZ}}{1 + (q\xi)^2} \quad (3)$$

where I_{OZ} is the scattering intensity at $q = 0$ and ξ the correlation length of concentration fluctuations.

I_{bkg} was left as a free fitting parameter. All SAXS data were modeled using the software SasView 5.06 [36].

Acknowledgments

We thank Y. Li (TU Munich) for help with the experiments. The synchrotron SAXS data were collected at beamline P12, operated by EMBL Hamburg at the PETRA III storage ring (DESY, Hamburg, Germany). We thank EMBL for excellent equipment. This work benefited from the use of the SasView application, originally developed under NSF award DMR-0520547. SasView contains code developed with funding from the European Union's Horizon 2020 research and innovation program under the SINE2020 project, Grant Agreement No. 654000.

References

1. Y. Mai and A. Eisenberg, "Self-Assembly of Block Copolymers," *Chemical Society Reviews* 41 (2012): 5969.

2. M. Karayianni and S. Pispas, "Block Copolymer Solution Self-Assembly: Recent Advances, Emerging Trends, and Applications," *Journal of Polymer Science* 2021 (1874): 59.

3. A. S. Lee, V. Bütün, M. Vamvakaki, S. P. Armes, J. A. Pople, and A. P. Gast, "Structure of pH-Dependent Block Copolymer Micelles: Charge and Ionic Strength Dependence," *Macromolecules* 35 (2002): 8540–8551.

4. S. Förster, V. Abetz, and A. H. E. Müller, "Polyelectrolyte Block Copolymer Micelles," *Advances in Polymer Science* 166 (2004): 173.

5. X. Wang, M. Goswami, R. Kumar, B. G. Sumpter, and J. Mays, "Morphologies of Block Copolymers Composed of Charged and Neutral Blocks," *Soft Matter* 8 (2012): 3036.

6. G. Kocak, C. Tuncer, and V. Bütun, "pH-Responsive Polymers," *Polymer Chemistry* 8 (2017): 144–176.

7. K. Kuperka, D. Patel, L. I. Atanase, and P. Bahadur, "Amphiphilic Block Copolymers: Their Structures, and Self-Assembly to Polymeric Micelles and Polymersomes as Drug Delivery Vehicles," *Polymers* 14 (2022): 4702.

8. T. Pelras, A. H. Hofman, L. M. H. Germain, A. M. C. Maan, K. Loos, and M. Kamperman, "Strong Anionic/Charge-Neutral Block Copolymers from Cu(0)-Mediated Reversible Deactivation Radical Polymerization," *Macromolecules* 55 (2022): 8795–8807.

9. V. Chrysostomou and S. Pispas, "Stimuli-Responsive Amphiphilic PDMAEMA-*b*-PLMA Copolymers and Their Cationic and Zwitterionic Analogs," *Journal of Polymer Science Part A: Polymer Chemistry* 56 (2018): 598–610.

10. M. Allmeroth, D. Moderegger, D. Gündel, et al., "HPMA-LMA Copolymer Drug Carriers in Oncology: An In Vivo PET Study to Assess the Tumor Line-Specific Polymer Uptake and Body Distribution," *Biomacromolecules* 14 (2013): 3091–3101.

11. M. Demetriou and R. Krasia-Christoforou, "Synthesis and Characterization of Well-Defined Block and Statistical Copolymers Based on Lauryl Methacrylate and 2-(Acetoacetoxy)ethyl Methacrylate Using RAFT-Controlled Radical Polymerization," *Journal of Polymer Science Part A: Polymer Chemistry* 46 (2008): 5442–5451.

12. F. A. Plamper, M. Ruppel, A. Schmalz, O. Borisov, M. Ballauff, and A. H. E. Müller, "Tuning the Thermoresponsive Properties of Weak Polyelectrolytes: Aqueous Solutions of Star-Shaped and Linear Poly(*N*,*N*-Dimethylaminoethyl Methacrylate)," *Macromolecules* 40 (2007): 8361–8366.

13. D. Cheng, N. Cao, J. Chen, X. Yu, and X. Shuai, "Multifunctional Nanocarrier Mediated Co-Delivery of Doxorubicin and siRNA for Synergistic Enhancement of Glioma Apoptosis in Rat," *Biomaterials* 33 (2012): 1170–1179.

14. A. M. Jhaveri and V. P. Torchilin, "Multifunctional Polymeric Micelles for Delivery of Drugs and siRNA," *Frontiers in Pharmacology* 5 (2014): 77.

15. H. Yu, C. Guo, B. Feng, et al., "Triple-Layered pH-Responsive Micelleplexes Loaded With siRNA and Cisplatin Prodrug for NF-Kappa B Targeted Treatment of Metastatic Breast Cancer," *Theranostics* 6 (2016): 14–27.

16. M. Chen, Y. Zhang, Z. Chen, S. Xie, X. Luo, and X. Li, "Synergistic Antitumor Efficacy of Redox and pH Dually Responsive Micelleplexes for Co-Delivery of Camptothecin and Genes," *Acta Biomaterialia* 49 (2017): 444–455.

17. Y. Li, T. Thambi, and D. S. Lee, "Co-Delivery of Drugs and Genes Using Polymeric Nanoparticles for Synergistic Cancer Therapeutic Effects," *Advanced Healthcare Materials* 7 (2017): 1700886.

18. Y. Jiang, T. M. Reineke, and T. P. Lodge, "Complexation of DNA With Cationic Copolymer Micelles: Effects of DNA Length and Topology," *Macromolecules* 51 (2018): 1150–1160.

19. X. Xie, Y. Chen, Z. Chen, et al., "Polymeric Hybrid Nanomicelles for Cancer Theranostics: An Efficient and Precise Anticancer Strategy for the Codelivery of Doxorubicin/miR-34a and Magnetic Resonance Imaging," *ACS Applied Materials & Interfaces* 11, no. 47 (2019): 43865–43878.

20. J. Faria, M. Magalhães, F. Veiga, A. C. Santos, and A. Figueiras, "Micelleplexes: A Promising Nanocarrier for the Transport of Genetic Material and Drugs," in *Advances in Pharmaceutical Biotechnology*, vol. 267, eds. J. K. Patra, A. C. Shukla, and G. Das (Springer Nature Singapore: Springer Singapore, 2020, Chap. 20).

21. M. Pereira-Silva, I. Jarak, C. Alvarez-Lorenzo, et al., "Micelleplexes as Nucleic Acid Delivery Systems for Cancer-Targeted Therapies," *Journal of Controlled Release* 323 (2020): 442–462.

22. I. Jarak, M. Pereira-Silva, A. C. Santos, F. Veiga, H. Cabral, and A. Figueiras, "Multifunctional Polymeric Micelle-Based Nucleic Acid Delivery: Current Advances and Future Perspectives," *Applied Materials Today* 25 (2021): 101217.

23. N. Naziris, N. Pippa, S. Pispas, and C. Demetzos, "Stimuli-Responsive Drug Delivery Nanosystems: From Bench To Clinic," *Current Nanoscience* 6 (2016): 166.

24. C. Demetzos, S. Pispas, and N. Pippa, eds., *Drug Delivery Nanosystems: From Bioinspiration and Biomimetics to Clinical Applications* (Singapore: Pan Stanford Publishing Pte. Ltd., 2019).

25. H. Cabral, K. Miyata, K. Osada, and K. Kataoka, "Block Copolymer Micelles in Nanomedicine Applications," *Chemical Reviews* 118 (2018): 6844–6892.

26. L. Zhou, M. Emenuga, S. Kumar, Z. Lamantia, M. Figueiredo, and T. Emrick, "Designing Synthetic Polymers for Nucleic Acid Complexation

and Delivery: From Polyplexes to Micelleplexes to Triggered Degradation," *Biomacromolecules* 23 (2022): 4029–4040.

27. C. E. Blanchet, A. Spilotros, F. Schwemmer, et al., "Versatile Sample Environments and Automation for Biological Solution X-ray Scattering Experiments at the P12 Beamline (PETRA III, DESY)," *Journal of Applied Crystallography* 48 (2015): 431–442.

28. A. Round, F. Felisaz, L. Fodinger, et al., "BioSAXS Sample Changer: A Robotic Sample Changer for Rapid and Reliable High-Throughput X-Ray Solution Scattering Experiments," *Acta Crystallographica Section D: Biological Crystallography* 71 (2015): 67–75.

29. M. A. Schroer, C. E. Blanchet, A. Y. Gruzinov, et al., "Smaller Capillaries Improve the Small-Angle X-Ray Scattering Signal and Sample Consumption for Biomacromolecular Solutions," *Journal of Synchrotron Radiation* 25 (2018): 1113–1122.

30. D. Franke, M. V. Petoukhov, P. V. Konarev, et al., "ATSAS 2.8: A Comprehensive Data Analysis Suite for Small-Angle Scattering from Macromolecular Solutions," *Journal of Applied Crystallography* 50 (2017): 1212–1225.

31. M. Kotlarchyk and S.-H. Chen, "Analysis of Small Angle Neutron Scattering Spectra From Polydisperse Interacting Colloids," *Journal of Chemical Physics* 79 (1983): 2461–2469.

32. G. Porod, "Die Röntgenkleinwinkelstreuung Von Dichtgepackten Kolloiden Systemen: I. Teil," *Kolloid Zeitschrift* 124 (1951): 83–114.

33. J. T. Koberstein, B. Morra, and R. S. Stein, "The Determination of Diffuse-Boundary Thicknesses of Polymers by Small-Angle X-Ray Scattering," *Journal of Applied Crystallography* 13 (1980): 34–45.

34. P. Schmidt, "Interpretation of Small-Angle Scattering Curves Proportional To A Negative Power of The Scattering Vector," *Journal of Applied Crystallography* 15 (1982): 567–569.

35. M. Shibayama, T. Tanaka, and C. C. Han, "Small Angle Neutron Scattering Study on Poly(N-Isopropyl Acrylamide) Gels Near Their Volume-Phase Transition Temperature," *Journal of Chemical Physics* 97 (1992): 6829–6841.

36. SasView, accessed August 2024, http://www.sasview.org.

Supporting Information

Additional supporting information can be found online in the Supporting Information section.